

MATERIALS SCIENCE

Toward ultimate nonvolatile resistive memories: The mechanism behind ovonic threshold switching revealed

Pierre Noé^{1*}, Anthonin Verdy¹, Francesco d'Acapito², Jean-Baptiste Dory¹, Mathieu Bernard¹, Gabriele Navarro¹, Jean-Baptiste Jager³, Jérôme Gaudin⁴, Jean-Yves Raty^{1,5*}

Fifty years after its discovery, the ovonic threshold switching (OTS) phenomenon, a unique nonlinear conductivity behavior observed in some chalcogenide glasses, has been recently the source of a real technological breakthrough in the field of data storage memories. This breakthrough was achieved because of the successful 3D integration of so-called OTS selector devices with innovative phase-change memories, both based on chalcogenide materials. This paves the way for storage class memories as well as neuromorphic circuits. We elucidate the mechanism behind OTS switching by new state-of-the-art materials using electrical, optical, and x-ray absorption experiments, as well as *ab initio* molecular dynamics simulations. The model explaining the switching mechanism occurring in amorphous OTS materials under electric field involves the metastable formation of newly introduced metavalent bonds. This model opens the way for design of improved OTS materials and for future types of applications such as brain-inspired computing.

INTRODUCTION

Chalcogenide materials have attracted much attention over the years owing to their broad array of applications, ranging from memories to optical or thermoelectric devices and so on. Among them, some chalcogenide compounds exhibit a unique portfolio of properties, which has led to their wide use for nonvolatile memory applications such as optical data storage or, more recently, phase-change memories (PCMs) (1). Besides a high infrared transparency window and large optical nonlinearities (2), some chalcogenide glasses (CGs) exhibit an uncommon conductivity behavior under high electric field, called the ovonic threshold switching (OTS) effect.

This OTS mechanism, discovered in the 1960s by Stanford R. Ovshinsky, consists of the reversible transition between a highly resistive state (OFF state) and a conductive state (ON state) when the voltage applied on the CG exceeds a critical threshold value, V_{th} (3). When the current is reduced below the holding current density, J_h , the selector recovers its high resistance state (1, 3–12).

Some chalcogenide materials are now considered as most promising for high-density, energy-efficient, nonvolatile resistive memories owing to their successful integration in high-density three-dimensional (3D) cross-point memory (CPM) arrays (13, 14). This can only be achieved by the addition of an active element, called selector, to each resistive memory cell. In the present case, the selector consists of a chalcogenide material, which allows the individual reading and programming of each memory point in the 3D memory network. This element should thus be able to provide not only a large enough current to reversibly switch the memory from the highly resistive (amorphous) RESET state to the highly conductive (and crystalline)

SET state but also a very low leakage current when the memory cell is unselected to avoid any undesired programming (see Fig. 1).

OTS materials are perfectly adapted for such a use (1, 4, 5), whereas conventional transistor fails, as demonstrated in the recently developed Optane technology from Intel/Micron (13). However, the underlying physical mechanism of the OTS effect is still unclear, as two different models have been proposed: The first one is based on a purely electronic excitation effect by tunneling in a hopping transport framework (6, 7), whereas the second one invokes a thermally assisted mechanism (8, 9) with a change of local structure or electric field-assisted formation of a metastable crystalline filament (10, 11) upon threshold switching.

Most known OTS materials are based on good glass formers such as Se and Se/Te CGs, all of them containing As as the network former (12). Originally, arsenic was introduced to improve the (meta) stability of these glasses against crystallization and external environment effects such as oxidation. However, the toxicity of As is notorious (15), and future technologies should thus replace it with less hazardous elements. This also creates a challenge for materials scientists and engineers.

In this work, we show how innovative As-free amorphous OTS thin films based on Se-rich GeSe glasses permit to achieve state-of-the-art OTS devices (16–18) with outstanding performance, such as well-adapted threshold voltage V_{th} , low subthreshold leakage current (I_{OFF}), and high endurance. In contrast to Ge-rich (19) or Sb-doped GeSe-based (20) OTS thin films, our Sb- and N-doped GeSe materials provide an ideal compromise between a high stability against crystallization, low V_{th} , and limited subthreshold currents that are critical for the development of higher-density and less-consuming 3D memories (1, 4, 5, 13).

We performed electrical measurements on test OTS devices as well as spectroscopic ellipsometry and x-ray absorption spectroscopy (XAS) measurements on the OTS films. We show that Sb and N atoms modify the structure of the Ge₃₀Se₇₀ (GS) glass in such a way that the OTS performance is strongly enhanced. Using *ab initio* molecular dynamics (AIMD) simulations, we provide a model for

Copyright © 2020 The Authors, some rights reserved; exclusive licensee American Association for the Advancement of Science. No claim to original U.S. Government Works. Distributed under a Creative Commons Attribution NonCommercial License 4.0 (CC BY-NC).

¹Université Grenoble Alpes, CEA, LETI, MINATEC Campus, 17 avenue des Martyrs, F-38000 Grenoble, France. ²CNR-IOM-OGG c/o ESRF–The European Synchrotron, 71 rue des Martyrs, F-38043 Grenoble, France. ³Université Grenoble Alpes, CEA, INAC, MINATEC Campus, 17 avenue des Martyrs, F-38000 Grenoble, France. ⁴CELIA, Université de Bordeaux, CEA, CNRS, UMR 5107, 351 Cours de la Libération, F-33405 Talence, France. ⁵CESAM-Physics of Solids Interfaces and Nanostructures, B5, Université de Liège, B4000 Sart-Tilman, Belgium.

*Corresponding author. Email: pierre.noe@cea.fr (P.N.); jyraty@uliege.be (J.-Y.R.)

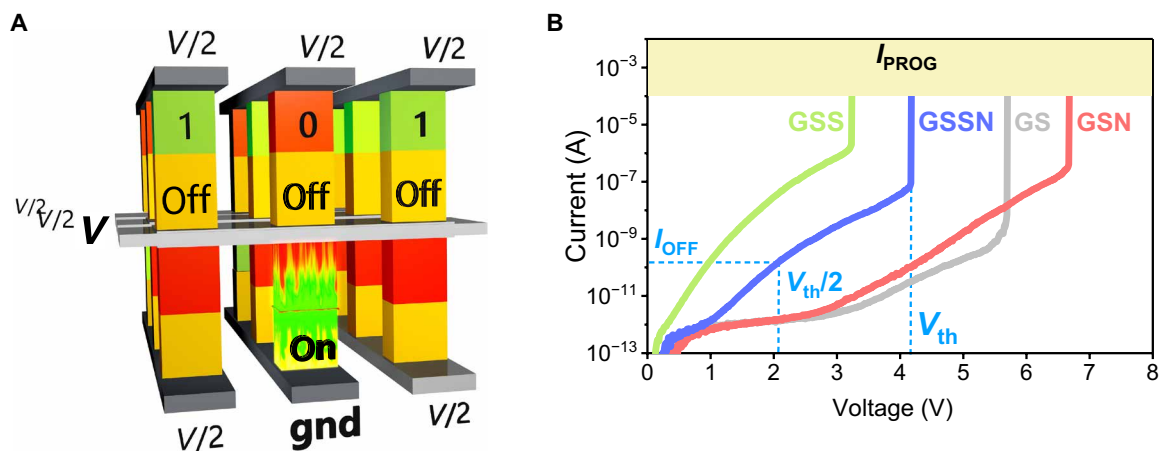


Fig. 1. Schematic representation of a resistive memory cell within a CPM network used in latest 3D memories. The cell is built by stacking a storage element (PCM) and an OTS selector. **(A)** Work principle of a PCM/OTS memory cell in a CPM structure. The structural state of the phase-change material of the PCM element is used to store the information: Bit 1 is coded by the low-resistance crystalline state (represented by a green block), and bit 0 is coded by the highly resistive amorphous state (red block). The selected PCM element initially in the RESET state can be programmed by applying on the PCM + OTS (yellow block) cell a voltage/current pulse high enough to switch the OTS selector ($V > V_{th}$) in its low-resistance SET state (green). To keep unaffected adjacent cells from undesired programming, a $V/2$ voltage is applied on contact electrodes (bit lines and word lines) of unselected cells, limiting the current to leakage current I_{OFF} [see (B)]. Contrary to phase-change materials, OTS materials are good glass formers to remain amorphous and highly resistive after each programming/reading operation. **(B)** I - V characteristics obtained from quasi-static (DC) measurement on prototypical GeSe-based OTS thin films in their as-fabricated state: GS, GSN, GSS, and GSSN. Whereas at low voltage the current flowing through the OTS material is very small (subthreshold current, or I_{OFF}), when the applied voltage exceeds threshold voltage (V_{th}), the OTS material experiences a spectacular drop of resistivity by several orders of magnitude, enabling high current flow. When this high voltage is removed, the OTS material recovers its highly resistive state.

the electrical switching mechanism. This new mechanism does not involve any melting of the glass but results from the change of bonding configuration toward what was recently described as metavalent bonding (MVB) (21, 22), which creates a strong electron delocalization upon high-electric field application. This approach also provides an insight into the nature of the OTS mechanism at the atomistic level. In contrast to all previous studies and analytical models that are based on phenomenological observations, a unified understanding of these properties from a microscopic point of view is proposed.

RESULTS

Electrical properties

On the basis of our previous studies of GeSe-based OTS materials (16–18), we here selected four prototypical compositions to evaluate the impact of the amorphous structure of CGs on their electrical behavior and performance in OTS devices: GS, GS doped with 8 atomic % (at %) of N (GSN), $\text{Ge}_{24}\text{Se}_{56}\text{Sb}_{20}$ (GSS), and GSS doped with 8 at % of N (GSSN) (see Materials and Methods).

The characteristics of nonlinear conductivity of all OTS thin-film materials studied are shown in Fig. 1B. All I - V curves exhibit a sudden jump in conductivity at a threshold value, V_{th} , that strongly varies with composition. Below this threshold, the current is significantly limited. This subthreshold conduction in amorphous chalcogenide has been extensively described and attributed to the Poole-Frenkel electronic transport and to a thermally assisted hopping between localized gap or tail states (6–12, 16–18). In the present case, GS and GSN exhibit a subthreshold current that is several orders of magnitude smaller than that of GSS and GSSN films.

It should be noted that the OTS materials measured here in electrical test devices are in their pristine, i.e., as fabricated, state to be in the same condition as the thin-film samples studied hereafter by

spectroscopic ellipsometry and XAS. In actual CPM devices, a first OTS cycle is usually applied to perform a “forming step” or “firing” (which induces small changes in subthreshold current values and V_{th}), after which all cycles yield the same I - V curves (23, 24).

All four materials undergo a drastic increase in current at the critical field V_{th} , the so-called OTS. The latter has been previously attributed to the filling of localized (or traps) states in the forbidden gap of the amorphous semiconductor and energy gain of electrons (6–9) or to the formation of an unstable conductive filament within the amorphous material (10, 11) upon high-electric field application. V_{th} is material dependent (16–20, 23), and in the present case, the addition of Sb and, to a lesser extent, N is drastically reducing its value in OTS selector devices.

We emphasize that Fig. 1B data are obtained using quasi-static DC measurements, which inevitably produce an electrical stress on the selector materials that is not present in memory devices. This stress tends to lower V_{th} (24) but with an amplitude that depends on the nature of the OTS materials; therefore, we used a pulsed data mode that is more relevant for the actual device to obtain the V_{th} values plotted in Fig. 2.

Among all compounds measured here, GSSN exhibits outstanding OTS performances featuring all properties required for selector applications (16–18, 24) while being fully compatible with standard CMOS (complementary metal-oxide semiconductor) fabrication processes. Among these properties, the endurance of GSSN has been shown to be excellent, as the OTS behavior is maintained over at least up to 10^9 cycles (17, 18). To understand the impact of Sb and N incorporation onto the electrical behavior of GS-based OTS materials, we probed the electronic properties of the OTS thin films using spectroscopic ellipsometry.

The optical bandgap determination is challenging in this class of amorphous semiconductor materials because of the large band tails and numerous defect states that are present in the bandgap of the

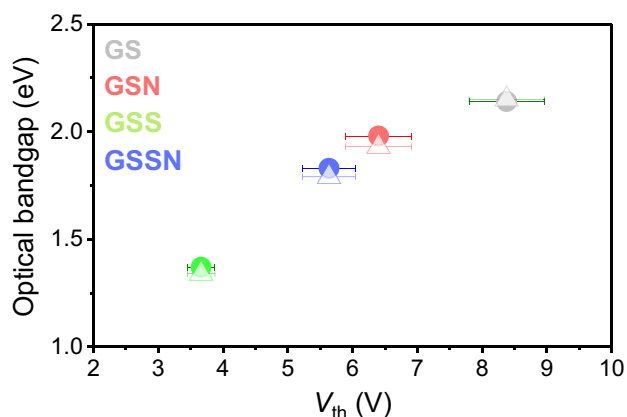


Fig. 2. Optical gap E_g^{opt} as a function of threshold voltage V_{th} in GeSe-based OTS materials. The optical bandgap values for the GeSe(Sb and N) OTS thin films were obtained by two different methods: from Tauc's plots (full symbols) and from a Cody-Lorentz (CL) model (empty symbols) used to fit the experimental ellipsometry data (see fig. S1). The V_{th} values were determined using pulsed mode on as-fabricated devices (see text).

electronic density of states (DoS). We therefore used two different methods (see Materials and Methods) to determine the optical bandgap values E_g^{opt} that we plot as a function of V_{th} in Fig. 2. The small deviation of V_{th} from the values visible in Fig. 1B data is, as expected, due to the use of a pulsed mode to determine V_{th} values plotted with E_g^{opt} , mode that limits the electrical stress and therefore tend to increase V_{th} (see Materials and Methods).

The correlation between E_g^{opt} and V_{th} is close to linearity, with a small deviation for GS [the obtained E_g^{opt} value is in excellent agreement with those found for similar $\text{Ge}_x\text{Se}_{1-x}$ glasses in (25)], which could be explained by the presence of a higher number of bandtail states and localized defect states, which are hardly evidenced by ellipsometry (see fig. S1). These electronic states are nevertheless influencing the electronic properties of the OTS material and thus possibly also their switching behavior. Sb and, to a lesser extent, N significantly reduce the bandgap of GS glass and thus V_{th} of OTS devices. As a result, the co-doping of GS glass with both Sb and N elements further enhances the OTS performance, combining an intermediate bandgap, and thus moderates V_{th} , with low subthreshold currents (I_{OFF}), while preserving the thermal stability that is compatible with CMOS integration processes (16–18).

As we have shown in a preliminary study (16), Raman and Fourier transform (FT) infrared measurements indicate the clear impact of Sb and N dopants onto the structure of amorphous GS. We thus analyzed the local order in GS glasses upon Sb and N doping using XAS to understand the link between structural changes at the atomic level and OTS properties.

Atomic structure of the amorphous materials

Figure 3 shows the EXAFS (extended x-ray absorption fine structure) spectra acquired at Ge, Se, and Sb K edges for all compounds (see Materials and Methods) and their FTs. No peak is visible at low R values (around 1.3 Å) in the FT spectra, where Ge—O bonds would contribute to the FT. Because Ge-based chalcogenide films are particularly prone to oxidation, these spectra confirm the absence of oxidation during and after the preparation process. This guarantees that measured quantities discussed hereafter are intrinsic

to the films and not related to any oxidation. Qualitatively, in all samples, Ge—Se bonds are dominating the FTs at Ge and Se edges. Ge and Sb atoms are highly influenced by the N addition, with the appearance of bonds with N atoms at short R values (centered at ~1.4 and ~1.6 Å in Ge and Sb FTs, respectively). On the contrary, Se exhibits a preferential link with Ge and Sb with no evidence of bond with N.

The quantitative analysis of the EXAFS data has been performed using a multishell model fitting procedure (see Materials and Methods for details). The experimental data could be modeled with up to three coordination shells (see fitting curves in fig. S2): Ge—Se, Ge—Sb, and Ge—N bonds at the germanium edge; Se—Ge and Se—Sb bonds at the selenium edge; and Sb—Sb, Sb—Se, and Sb—N bonds at the antimony edge. The results of the quantitative analysis at the three K edges are summarized in table S1.

The mean Ge—Se distances derived from the Ge—K edge ($R_{\text{Ge-Se}} = \sim 2.38$ Å) or from the Se—K edge ($R_{\text{Se-Ge}} = \sim 2.38$ Å) are similar in all compounds, as they are (within SE) almost unaffected by Sb and N introduction (table S1). The atomic coordination numbers (CNs) are plotted in Fig. 4. In GS, the Ge—Se coordination number $N_{\text{Ge-Se}}$ is slightly lower than 4 (~3.8) and $N_{\text{Se-Ge}}$ is slightly higher than 2 (~2.3). The slight overcoordination of Se atoms is only resulting from the impossibility of XAS analysis to distinguish Se—Se from Se—Ge scattering paths, the electronic density of Ge and Se atoms being too close. As a result, the Se—Ge CNs also include the contribution of Se—Se bonds, as highlighted in Fig. 4 when comparing with the CNs found in AIMD models. These observations are in good agreement with previous reports on $\text{Ge}_x\text{Se}_{1-x}$ glasses, with $x < 33$ (26–31). The amorphous network of GS has been well described by tetrahedral $\text{Ge}(\text{Se}_{1/2})_4$ units connected by an edge (edge sharing) or a corner (corner sharing) (26–31).

Despite the absence of variations in the length of Ge—Se bonds, the addition of N and Sb reduces the Ge—Se CN, keeping the overall Ge and Se coordination relatively constant, because of the appearance of Ge—N (seen at the Ge edge) and Sb—Se/Se—Sb (seen at the Sb and Se edges) bonds. Ge—N bonds are found around 1.84 Å (table S1), which is in good agreement with values from the literature (32, 33).

Last, one of the most interesting features derived from these data is the appearance of wrong (Ge—Sb) and homopolar (Sb—Sb) bonds in case of Sb introduction, which is avoided when N is also introduced in the GS glass. A similar observation was made in a previous study of Sb-rich Ge—Sb—Se bulk glasses by neutron diffraction, x-ray diffraction, and XAS (34). This result is of major importance as we will discuss in the following.

DISCUSSION

At this point, one can wonder about the main parameters that could help tailor the CGs' amorphous structure and composition to optimize their electronic and OTS performance. Because of its high stability against crystallization, one could think that GS would be the best OTS material, among $\text{Ge}_x\text{Se}_{1-x}$ glasses (16). However, this is not the case, as its V_{th} is too high for memory crossbar applications and its cycling endurance is poor (16). The XAS analysis of the four prototypical GeSe-based glasses can give us an insight into the origin of OTS property improvement.

First, the introduction of Sb in the GeSe glass leads to the formation of Sb—Se bonds. These induce electronic states that reduce the bandgap of the material as shown in Fig. 2, which is in good agreement

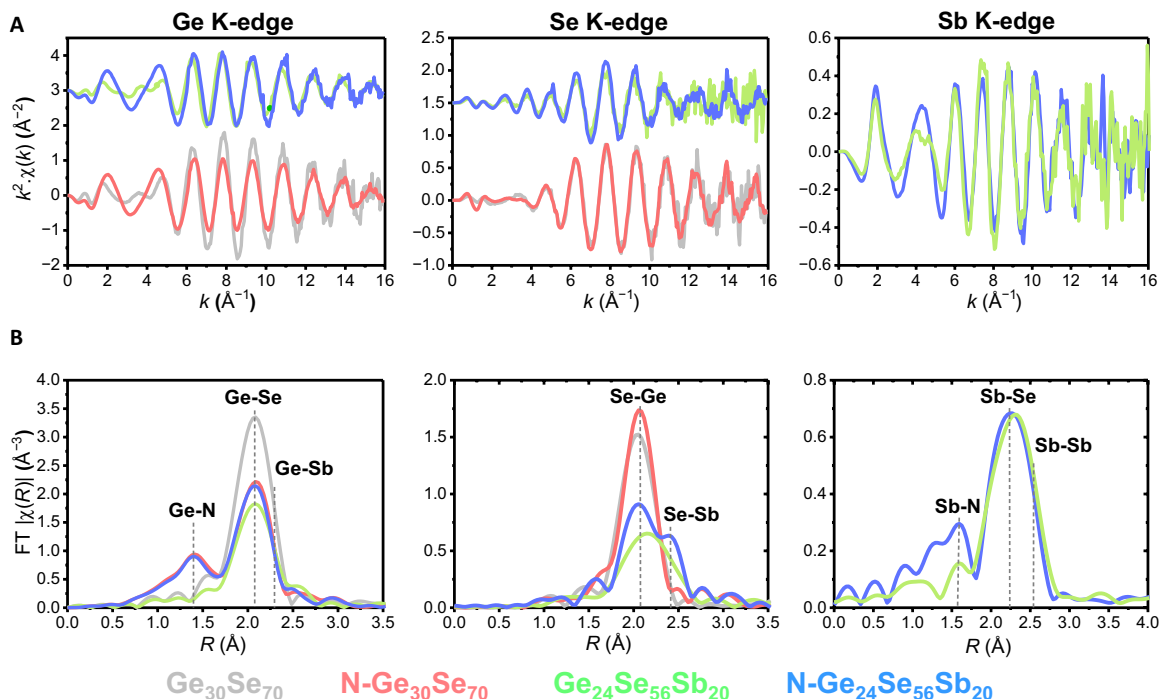


Fig. 3. Analysis of the local structure of GeSe-based OTS thin films by EXAFS at Ge, Sb, and Se K edges. (A) EXAFS (extended x-ray absorption fine structure) experimental spectra acquired at the Ge, Se, and Sb K edges of the four prototypical GeSe(Sb and N) OTS thin-film samples. (B) FTs of the experimental EXAFS spectra. The vertical dashed lines mark the position of the Ge–Se (Se–Ge), Sb–Se (Se–Sb), Ge–N, and Sb–N bonds (for fitting of experimental data, see Materials and Methods and fig. S2).

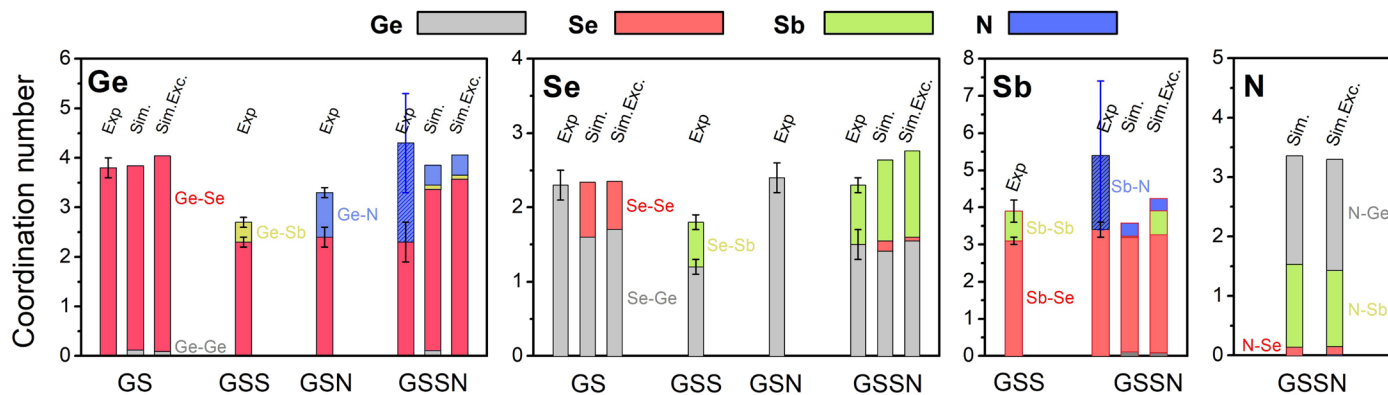


Fig. 4. Atomic CNs for GS, GSS, GSN, and GSSN OTS materials obtained from XAS experiment and calculated by AIMD simulations. The CNs were obtained from quantitative analysis of XAS experimental data in Fig. 3 (Ge, Sb, and Se atoms) and compared with those derived from simulation of GS and GSSN AIMD models (Ge, Sb, Se, and N atoms) in either the initial state (Sim.) or the excited state (Sim. Exc.). An excellent agreement is found between CNs of experiment (see also Materials and Methods, fig. S2, and table S1) and those from GS and GSSN AIMD models (see Materials and Methods, the “OTS model” section, and table S2). In the simulations, one notes that, upon excitation, the CNs of the Ge, Se, and Sb atoms in both GS and GSSN models (Sim. Exc.) increase slightly. The origin of such an effect is of utmost importance regarding the OTS mechanism (see text).

with previous studies (20, 35). The introduction of Sb has nevertheless two major drawbacks that limit its potential for applications.

Under thermal stress, Sb_2Se_3 and Se phases tend to easily segregate in the amorphous film and crystallize, resulting in a poor thermal stability of the material and failure of OTS devices (16). Second, Sb introduction in GS results in the formation of wrong (Ge–Sb) and homopolar (Sb–Sb) bonds. These bonds are known to significantly affect the electronic DoS of amorphous chalcogenide with introduction of bandtail and midgap states (18, 36–39). These defect

states have been held responsible for an increase in the subthreshold current I_{OFF} due to an increase in the Poole and Poole-Frenkel transport (6, 7, 9). The increased density of electronic defect states and the reduction of the energy barriers for electrons promote hopping of the electronic carriers, therefore increasing the electrical conductivity of the OTS material. On the contrary, the introduction of N in GSS glass prevents these wrong and homopolar bonds due to the preferential formation of Ge–N and Sb–N bonds, as evidenced by XAS (Fig. 3 and table S1). This addition not only limits I_{OFF} but also improves

significantly the thermal stability against recrystallization due to an increased glass rigidity. It has been established that introducing light elements in amorphous chalcogenide enhances significantly their amorphous phase stability against crystallization (1, 40–44). In case of C and N, this effect has been attributed to an increased mechanical rigidity associated to changes in local atomic arrangement (41, 42, 44). The GSSN thus ideally combines a well-adapted V_{th} and low leakage

current (16), as well as a high stability and cycle endurance (17), while being fully compatible with current CMOS technological processes [back end of line (BEOL) compatibility] (18).

OTS model

To understand the relation between local atomic structure and the different performances of the glasses, we performed AIMD simulations.

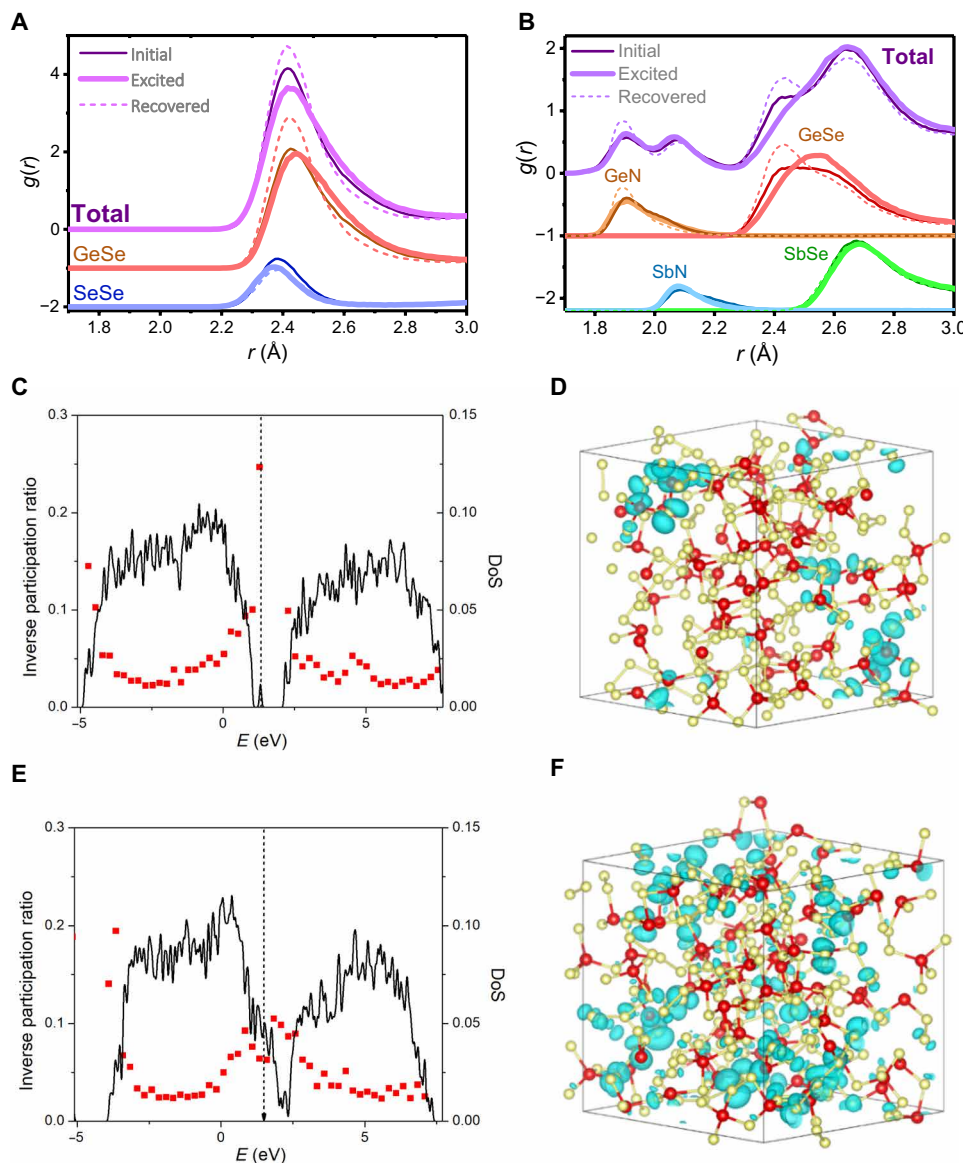


Fig. 5. Evolution of the amorphous structure and electronic DoS of GS and GSSN OTS materials before, during and after electronic excitation. PDF of (A) GS and (B) GSSN before, during, and after excitation, as well as electronic DoS and instantaneous snapshots of amorphous GS in the initial (C and D) and excited state (E and F). Partial contribution of the different bonds to the total PDF (purple lines) of (A) GS and (B) GSSN is shown. The continuous, bold, and dashed lines indicate the OTS materials in their pristine, excited, and recovered states, respectively. The excited and recovered states correspond to the OTS materials upon electronic excitation to mimic the effect of an electric field application and after stopping the electronic excitation and annealing of the ions at 300 K. (C and E) Electronic DoS of GS model in its initial state (C) and in the excited state (E). The initial semiconducting material (C) has a large bandgap (the Fermi level is indicated by the dashed line) with some localized defect states and bandtails, as evidenced by plotting the inverse participation ratio (IPR; shown by the red dots; IPR values are averaged over states within 0.25 eV of the reference value). In the metallic excited state (E), as the bandgap closes, the DoS increases strongly and the IPR values drop around the Fermi level. The delocalization of states indicated by this drop in the IPR value around E_F is illustrated on the atomic snapshots displayed in (D) and (F), in which the electronic Kohn-Sham states at the Fermi level are plotted as blue isosurface curves (drawn at 15% of their maximal value). A strong localization of electrons is observed in the initial insulating state (D), in contrast to the generalized electronic delocalization visible in the excited state (F). The huge increase in conductivity upon electric field application observed at threshold switching in OTS materials can then be explained by the strong delocalization of the electronic states around E_F wave functions.

For this purpose, we chose GS and N-doped GSS glasses as prototypical models, as these compositions yield very different threshold voltages for OTS. The simulations were performed with 240 atoms and atomic compositions $\text{Ge}_{72}\text{Se}_{168}$ and $\text{Ge}_{55}\text{Se}_{127}\text{Sb}_{46}\text{N}_{12}$ (see Materials and Methods for details and the two snapshots of the computed models shown in fig. S3). Before interpreting the AIMD results, we first validate the amorphous structures by confronting simulations with experimental data, such as the CNs and interatomic distances obtained from XAS. The analysis of the pair distribution function (PDF) of both systems is shown in Fig. 5 (A and B).

We note that there is an excellent agreement between the local environments around the different atomic species (Ge, Se, and Sb) in the simulated structures and those determined by fitting of the EXAFS spectra (see tables S1 and S2 and fig. S3). This conclusion is well supported when comparing experimental and simulated CNs for the GS and GSSN materials (Fig. 4). As usually observed though, the generalized gradient approximation (GGA) exchange functional tends to yield overestimated first neighbors' distances; however, all trends are well reproduced. Now, to understand the uncommon conductivity behavior of these compounds, we simulated the impact of an electric field application using a forced occupation of the excited electronic states (see Materials and Methods).

Until now, various models have been proposed to explain the OTS mechanism. Using our method, we could observe a significant modification of the local order (Fig. 5, A and B) upon excitation and modification that does not involve any melting of the structure. The PDF, using the same degree of excitation, differs for the pristine glass in its excited state and after recovery when the amorphous structure has relaxed.

The main changes observed upon excitation, particularly for GSSN, are found for bonds involving the chalcogen element (Se) with an increase in the Ge-Se distance. One can wonder whether these changes in the amorphous structure are sufficient to produce a significant impact on the electronic properties of the OTS materials.

Therefore, we computed the electronic DoS of GS and GSSN models (see Fig. 5, C and E, for GS and Materials and Methods). As illustrated for GS (Fig. 5, D and F), states around E_f delocalize upon

excitation and cannot really be considered as defect states anymore. This is indicated by the strong lowering of the inverse participation ratio (IPR) values for states inside and around the electronic gap (see Materials and Methods). The detailed investigation shows that the main changes in GS are the creation of delocalized states along Se-Se bonds and in planar Ge-Se motifs (see fig. S4). The latter observation for our GS compound model is different from the bandtail model recently proposed in (45). In this model, Ge-Ge bonding configurations were proposed to be at the origin of creation of conduction band tail states that lead to the nonlinear conduction of Ge-rich $\text{Ge}_x\text{Se}_{1-x}$ OTS materials. Actually, we found that the main effect of electronic excitation is to increase the degree of bond alignment (see Fig. 6). In GS, this is due to the opening of some angle within an initially tetrahedral coordination shell of Ge, whereas in GSSN the effect is stronger and is due to the quasi-alignment of two bonds, one of which involving a neighbor bound at an intermediate distance (2.8 to 3.1 Å) (Fig. 6A). A corresponding effect is found around Sb atoms in GSSN (Fig. 6B).

This bond alignment is expected to introduce more and more conductive channels at the Fermi level of the amorphous semiconductor. Initially, this bond alignment was invoked to explain the strong contrast between amorphous and crystalline phase-change materials phases (46, 47), and bonding was named “resonant bonding,” as in graphite. As shown for crystalline GeTe, the progressive alignment makes the material more and more conductive and translates into the appearance of anomalous effective charges and large atomic polarizabilities. Most recently, it was shown (21, 22) that such an alignment is responsible for a partial occupation of bonds and specific properties that differ from those of graphite, and the concerned materials have been qualified as “metavalent.” This bond alignment inside the amorphous structure is thus expected to introduce more and more conductive channels around the Fermi level. To establish a comparison with these observations made for crystals, we computed the Born effective charges Z^* using density functional perturbation theory (see Materials and Methods) for the present glass models.

The results are shown in Fig. 6. Extremely large effective charges are created for Ge upon excitation, however, with a different origin in

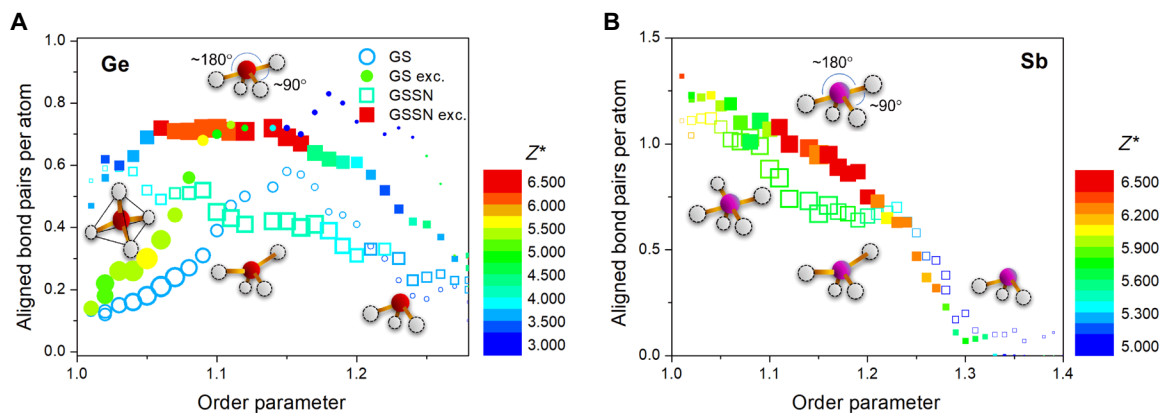


Fig. 6. Evolution of bond alignment in GS and GSSN before and during excitation as well as the effect on bond polarizability. Although the global topology of the network is conserved upon excitation, important changes can be observed on the proportion of quasi-aligned bonds (two bonds deviating by less than 20°), as plotted for (A) Ge and (B) Sb atoms. The x axis represents an order parameter (ratio of the fourth interatomic distance to the average of the first three), for which typical structures are shown as insets (for details, see Materials and Methods) (36). The color of the symbol is given by the magnitude of the maximum value of the Born effective charge, Z^* , eigenvalue, which is a measure of bond polarizability (see color scale bars on the right of graphs). A large increase in Z^* is observed upon excitation for atoms that tend to have two aligned bonds. Empty and plain symbols are used for the amorphous material before and during excitation, respectively. Circles and squares are used for GS and GSSN, respectively. Symbol size is proportional to the average number of data points. The Z^* values for Se atoms are shown in fig. S5.

GS and GSSN. In GS, the effect is carried by tetrahedral units, whereas in GSSN it is carried more by distorted octahedral (36). This polarizability increase is associated with the improved alignment of bonds at an intermediate distance. In GSSN, the same effect is evidenced for Sb upon excitation—the enhanced octahedral character of the atoms causing a further increase in Z^* from the already large anomalous values observed in the initial glass.

The latter observation gives a clue on the origin of the OTS mechanism. It shows that carrier hopping induced by an electrical field application can induce a metastable structural change when the excitation level is sufficient to enable electrons to start populating the conduction states. The difference in the magnitude of this effect in between GS and GSSN systems is mostly related not only to their difference in bandgap (see Fig. 2 and fig. S1) and defect density, as highlighted in Figs. 1 and 2, but also to their ability to locally align bonds without requiring atomic diffusion.

It is noteworthy that after recovery, the amorphous structure is irreversibly modified in comparison with the initial pristine state. This is also very instructive regarding the forming step issue in OTS devices. It is usually observed in selector devices that, after the first OTS cycle, the electronic properties of the OTS evolve with, for instance, a decrease in V_{th} , requiring a so-called forming or firing step before OTS device operation (23, 24). The atomistic view of OTS given here by simulation shows that such an effect could be reasonably attributed to the result of a structural relaxation of the glass induced by the electronic excitation. This is very clear on the Ge-Se partial PDF (Fig. 5A). The initial state has a bimodal distribution with dominant contributions of comparable importance around 2.41 and 2.57 Å. The excited state is unimodal, and so is the recovered glass, in which part of the 2.57 Å neighbor subshell has merged into the 2.41 Å subshell. A detailed investigation of the structure shows that this change comes from transformation of some fourfold bonded Ge atoms, with neighbors forming 90° and 180° angles [similar to what is found in amorphous GeTe before aging (36)] into tetrahedrally bonded Ge. The energy of recovered amorphous models is lower than that of their pristine amorphous counterpart. Therefore, the energy given by excitation permits to overcome local energy barriers and the relaxation of the glass toward a more stable structure afterward, although the system never gets diffusive (liquid).

To summarize, AIMD simulation of excited GS-based OTS materials evidences a significant structural change of the amorphous structure, with a local ordering of Ge—Se (and Sb—Se in the GSSN system) bonds as the starting mechanism for OTS switching. The present model allows some consensus between the previously invoked electronic and structural model mechanisms because we show that both aspects are involved in the OTS switching mechanism described here. Besides, it must be emphasized that the present model does not exclude any further thermal effect after this electronically induced structural change under high electric field. After switching the material into its highly conductive glassy state, it is reasonable to consider that under prolonged exposition to a high current flow, the material would finally melt around an initial conductive channel as it has been proposed in the literature (10, 11). Besides, this could also explain the huge hysteresis in the current-voltage characteristic observed in OTS materials when the applied voltage is decreased to recover the highly resistive amorphous phase. After OTS switching, the highly resistive state can be maintained at voltage under V_{th} until the holding current density (J_h) is reached. When the current is reduced under J_h , the materials recover its highly resistive state, which could be

ascribed to solidification of the liquid filament and recovery of amorphous state electronic properties.

CONCLUSION

In conclusion, despite a lack of understanding of its physical origin in the past 50 years since its discovery, the unique threshold-switching phenomenon observed in Se- and Te-based amorphous chalcogenides upon electrical field application has nevertheless led recently to a major technological breakthrough in the memories field. The latter enabled the advent of high-density 3D nonvolatile resistive memories because of the association of a PCM element and an OTS selector, both based on chalcogenide materials (4, 5, 13). In that context, we have shown that tailoring the amorphous structure of GS-based thin films by N and Sb incorporation produces highly performant OTS materials, as demonstrated in selector devices (16–18, 24). Because of the investigation of amorphous structure of prototypical chalcogenide thin films coupled with analysis of their electronic properties and their OTS behavior upon electric field application, we made it possible to draw design rules to optimize further the OTS properties of amorphous chalcogenides. First, controlling the number of homopolar and wrong bonds is demonstrated to be a key parameter to control subthreshold leakage current, which is the main limitation toward an increase in crossbar array sizes in 3D memory devices, whereas controlling the bandgap of the material permits to adjust the value of the threshold voltage. Moreover, increasing the rigidity of the amorphous structure by introducing covalently bonded element such as N atoms improves the amorphous phase stability against crystallization and therefore the endurance of the OTS selector.

While subthreshold conduction mechanisms in CGs are now well understood with more and more accurate models to describe experimental observations, the underlying physical mechanism at play during the OTS is still highly debated. Using AIMD simulations validated by all the above experimental investigations, we have been able to relate the OTS mechanism to subtle structural rearrangements of the amorphous phase upon high electric field application. The simulated electronic excitation of the glasses results in structural reordering, with bond alignment and appearance of local structural motifs reminiscent of the MVB that has been recently described in crystalline chalcogenide phase-change materials (21, 22). The latter are therefore responsible for a huge change of electronic DoS accompanied by a huge increase in electronic conductivity of the materials.

In addition, the present OTS model tends to establish for the first time the common link between chalcogenide materials belonging to phase-change materials and those from the OTS family. In both systems, the MVB mechanism is at the origin of the unique properties that led to the recent breakthrough in nonvolatile memory field because of the coupling of a PCM-resistive cell and of an OTS selector. As evidenced here, the main difference between phase-change materials and OTS materials can be found in their ability to stabilize the MVB mechanism and in the energy barrier to crystallization.

Observing in situ the structural features of OTS switching remains a challenge. First, the limited volume of OTS material within the device requires the use of characterization techniques, which can probe areas as small as a few tens of square nanometers. Moreover, because of the use of high electrical fields, the OTS has to be triggered by electrical pulses of a few tens of nanoseconds, therefore limiting the in situ analysis to time-resolved experiments with nanosecond

resolution. Nevertheless, the recent development of ultrahigh brilliance and time-resolved sources such as x-ray free electron lasers may give us the opportunity in the near future to measure the structural changes accompanying OTS by time-resolved nanoprobe. In a very recent study (48), a similar approach has been successfully used to evidence, for the first time, a liquid-liquid phase transition in phase-change materials by femtosecond diffraction.

The present experimental and simulation findings could be used to design chalcogenide materials with improved properties for applications exploiting their unique nonlinear behavior under an electric field. For instance, the unique nonlinear behavior under optical or electrical excitation could lead to the development of performant new neuromorphic devices to mimic signal processing of biological neurons beyond von Neumann computing schemes (49, 50).

MATERIALS AND METHODS

Thin-film deposition and OTS devices

The GeSe(Sb and N) thin films were deposited in an industrial magnetron sputtering cluster tool on 200-mm Si-based substrates. The introduction of Sb and N elements in Se-rich GeSe (GS) thin films has been achieved by reactive magnetron co-sputtering from Sb and GS targets under reactive Ar and N₂ atmosphere. Film thicknesses, compositions, and deposition homogeneity over the 200-mm substrate were controlled by x-ray reflectivity and wavelength-dispersive x-ray fluorescence. In this work, four different prototypical compositions were selected to study the impact of the amorphous structure of CGs on the electrical behavior and performance in devices: GS, GSN, GSS, and GSSN. For XAS analysis, film thicknesses were fixed to 200 nm, and immediately after deposition, all films were capped in situ by a 10-nm-thick SiN layer to prevent oxidation. For electrical measurements, GeSe(Sb and N) thin films were integrated in OTS selector test devices, as detailed in (16).

Integration and electrical characterization of OTS selector devices

For OTS selector device fabrication, an OTS layer of a few tens of nanometers was deposited on top of a 350-nm-diameter W plug used as the bottom electrode contact. Then, immediately after deposition of the OTS layer, a TiN top electrode was deposited without breaking the vacuum, preventing oxidation of the OTS layer.

I-V characteristics of OTS devices were measured in DC mode with an HP 4156 analyzer. A current compliance of 1 mA was used. Because DC measurements involve an important electrical stress that lowers the threshold voltage, the latter was extracted by pulsed mode measurement using an HP 81110 pulse generator. An external resistance of 1 kilohm was used to limit the current after switching of the OTS in the ON state. The switching in the ON state was detected by probing the voltage that drops upon OTS using a Tektronix TDS 744 oscilloscope plugged on the external resistance.

Spectroscopic ellipsometry

Ellipsometry measurements were performed on J.A. Woollam M-2000 equipment working in the 190- to 1790-nm range. Data were acquired at three incident angles (55°, 65°, and 75°). The collected data were analyzed and modeled using the WVASE software. Dielectric functions, optical constants (refractive index *n* and extinction coefficient *k*), and absorption coefficient *α* as a function of the photon

energy in the 0.73- to 6.5-eV range were extracted from modeling of spectroscopic ellipsometry data using a Cody-Lorentz (CL) model. Because of an improved account of the Urbach absorption, the CL model was shown to be more accurate to describe our materials than the commonly used Tauc-Lorentz model, even if the latter has been well adapted for amorphous semiconductors. The CL model permitted to get an excellent match with the CG optical behavior in transparency and interband absorption regions. It must be emphasized that the chalcogenide bandgap absorption region is complex to model mathematically, and combination of several models has been used in previous literature to obtain accurate fits in this spectral range (51–53). From the analysis of the absorption coefficient *α* as a function of the photon energy as well as the *E_g* extracted from the CL fitting model, one can deduce an estimation of optical bandgap for our amorphous semiconductor thin films as a function of composition (see Fig. 2). We emphasized that the thus obtained bandgap values are in excellent agreement with previous literature on similar materials (54, 55).

X-ray absorption spectroscopy

XAS experiments on the 200-nm-thick GeSe(Sb and N) thin-film samples were performed on LISA-BM08 beamline at the European Synchrotron (ESRF) (56). XAS data at the Ge-K (*E* = 11,103 eV), Se-K (*E* = 12,654 eV), and Sb-K (*E* = 30,490 eV) edges were collected in the grazing incidence mode with an incidence angle of 4° to increase the beam footprint and thus measurement sensitivity. The x-ray optics consisted of an LNT (Liquid Nitrogen Temperature)-cooled monochromator equipped with a pair of Si(111) crystals for energy selection, and vertical focusing was achieved using a pair of cylindrical Pd-coated mirrors with an incidence angle of 2 mrad. Data collection was carried out with fluorescence mode using a 12-element energy-resolving high-purity Ge detector or a Si photodiode.

The FTs of EXAFS data were carried out in the interval *k* = [3–16] Å⁻¹, and the fits were carried out in *R* space on *k*²-weighted spectra in the interval *R* = [1–2.5], [1–3], and [1–2.8] Å for Ge, Se, and Sb K edges, respectively.

For quantitative analysis of the EXAFS, data were modeled using multishell models at the Ge, Se, and Sb K edges (for Ge, Se, and Sb K edges, the following paths were respectively used: Ge-Se/Ge-Sb/Ge-N, Se-Ge/Se-Sb/Se-N, and Sb-Sb/Sb-Se/Sb-N). An amplitude calibration factor (including the amplitude reduction factor *S₀*² plus possible systematic errors in the amplitude of the theoretical signal) derived from the spectra of different compounds (Ge bulk, GaAs, GaN, GeO₂, and GeSb) was used to correct the apparent amplitude and resulted to be 1.1(1) for Ge, 0.9(1) for Se, and 0.65(5) for Sb. Self-absorption effects were taken into account using the Booth method as implemented in the Athena code (57), although they have a very moderate effect (<10%).

Ab initio simulations

The ab initio simulations were performed using the Vienna Ab initio Software Package (58), using the GGA-PBE (Perdew-Burke-Ernzerhof) exchange functional (59), PAW (projector augmented wave) potentials (60, 61), and 520-eV plane wave cutoff. We adopted a melt-quench procedure to produce the amorphous structures, the density of which was adjusted during the quench to limit the residual stress. In each case, we produced five independent trajectories and averaged the results. The 240-atom amorphous models were obtained by performing simulated annealing (from 1000 to 300 K in 100 ps after

initial equilibration at 3000 K), with a time step of 1 fs for GSSN and 3 fs for GS and a Nosé thermostat. The density was optimized at regular intervals during the quench to yield zero residual stress in the final amorphous structure.

The electronic DoS were computed using the HSE06 hybrid functional (62) to improve the determination of the gap, which is strongly undervalued with density functional theory (DFT)–PBE.

The structure of the glasses upon OTS switching was modeled by fixing the occupation of electronic states, forcing the initial excitation of valence electrons close to E_F by 1 eV and keeping the occupation of the involved states fixed (we set the occupation to $1/2$, which ensures the self-consistent field convergence) after that, which allowed significant electron-phonon coupling. Our approach, though indirect, forces excitation from valence to excited states, somehow mimicking the increase in the Fermi energy with applied voltage at the electrodes. This method is different from that fixing a Fermi electron distribution with a high electronic temperature. In that case, the electron state occupation depends on energy (a gap could open, for instance), which is not the case in our simulations. The dynamics was performed during 30 ps in the excited states and another 30 ps after stopping the excitation to recover a low-energy amorphous structure.

The Born effective charges Z^* were computed using density functional perturbation theory (63). The concept of effective charges is not relevant for metals, and it is thus not possible to compute those in the excited state during OTS. To overcome this, we instantaneously froze the system in the excited state and initiated a short atomic relaxation, stopping as soon as the opening of a gap was observed (we chose a value of 0.1 eV as a criterion). This allowed us to compute Z^* values and relate the eventual anomalies to structural features.

The IPR was computed for each electronic state by effectively measuring a number of atomic orbital projections, with normalization (we included s and p projections). A value of 1 would mean perfect localization, and a value of $1/N$ would mean perfect delocalization (N is the total number of possible atomic orbital projections in the simulation box). The IPR values for deep valence states indicated that delocalized, bulk-like, states have IPR values equal to ~ 0.01 .

The order parameter used to plot the fraction of aligned bond pairs and the Born effective charge Z^* for Ge, Sb, and Se atoms is the ratio of the distance of an atom with the fourth closest atom and the average of the distances with the three other closest atoms. A value of 1 is, in the case of Ge, obtained for a perfect tetrahedron, whereas a larger value is indicative of a threefold bonded atom, and intermediate values can be associated to distorted octahedra (as shown in the schematic structural motifs). For instance, for Sb in GSSN, the average structure is a distorted octahedron so that a value of 1 corresponds to an octahedron with four short distances and two longer distances.

SUPPLEMENTARY MATERIALS

Supplementary material for this article is available at <http://advances.sciencemag.org/cgi/content/full/6/9/eaay2830/DC1>

Fig. S1. Ellipsometry data for the GS amorphous film and Tauc's absorption plots of OTS thin films.

Fig. S2. EXAFS data and fitting curves for GS and GSSN thin film samples.

Fig. S3. Instantaneous snapshots of GS and GSSN amorphous models obtained from AIMD simulations.

Fig. S4. Instantaneous snapshots and selected details of the electronic density at the Fermi energy for amorphous GS and GSSN in their excited state.

Fig. S5. Evolution of the dynamical charge in initial state and upon excitation for Se in GS and GSSN.

Table S1. Quantitative results of the XAS data analysis at Ge, Se, and Sb K edges.

Table S2. Coordination numbers and interatomic distances for GS and GSSN AIMD models.

REFERENCES AND NOTES

1. P. Noé, C. Vallée, F. Hippert, F. Fillot, J.-Y. Raty, Phase-change materials for non-volatile memory devices: From technological challenges to materials science issues. *Semicond. Sci. Technol.* **33**, 013002 (2018).
2. D. Tsiulyanu, M. Ciobanu, Room temperature a.c. operating gas sensors based on quaternary chalcogenides. *Sens. Actuators B* **223**, 95–100 (2016).
3. S. R. Ovshinsky, Reversible electrical switching phenomena in disordered structures. *Phys. Rev. Lett.* **21**, 1450–1453 (1968).
4. G. W. Burr, R. S. Shenoy, K. Virwani, P. Narayanan, A. Padilla, B. Kurdi, H. Hwang, Access devices for 3D crosspoint memory. *J. Vac. Sci. Technol. B* **32**, 040802 (2014).
5. C. Kügelner, M. Meier, R. Rosezin, S. Gilles, R. Waser, High density 3D memory architecture based on the resistive switching effect. *Solid State Electron.* **53**, 1287–1292 (2009).
6. D. Ielmini, Y. Zhang, Analytical model for subthreshold conduction and threshold switching in chalcogenide-based memory devices. *J. Appl. Phys.* **102**, 054517 (2007).
7. D. Ielmini, Threshold switching mechanism by high-field energy gain in the hopping transport of chalcogenide glasses. *Phys. Rev. B* **78**, 035308 (2008).
8. A. Redaelli, A. Pirovano, A. Benvenuti, A. L. Lacaita, Threshold switching and phase transition numerical models for phase change memory simulations. *J. Appl. Phys.* **103**, 111101 (2008).
9. M. Le Gallo, A. Athmanathan, D. Krebs, A. Sebastian, Evidence for thermally assisted threshold switching behavior in nanoscale phase-change memory cells. *J. Appl. Phys.* **119**, 025704 (2016).
10. I. V. Karpov, M. Mitra, D. Kau, G. Spadini, Y. A. Kryukov, V. G. Karpov, Evidence of field induced nucleation in phase change memory. *Appl. Phys. Lett.* **173501**, 92 (2008).
11. V. G. Karpov, Y. A. Kryukov, I. V. Karpov, M. Mitra, Field-induced nucleation in phase change memory. *Phys. Rev. B* **78**, 052201 (2008).
12. W.-C. Chien, C.-W. Yeh, R. L. Bruce, H.-Y. Cheng, I. T. Kuo, C. Yang, A. Ray, H. Miyazoe, W. Kim, F. Carta, E. Lai, M. J. Brightsky, H. Lung, A study on OTS-PCM pillar cell for 3-D stackable memory. *IEEE Trans. Electron Devices*. **65**, 5172–5179 (2018).
13. J. Choe, Intel 3D XPoint memory die removed from Intel Optane™ PCM (phase change memory) (TechInsights Inc., 2017); www.techinsights.com/about-techinsights/overview/blog/intel-3d-xpoint-memory-die-removed-from-intel-optane-pcm/.
14. T. Kim, H. Choi, M. Kim, J. Yi, D. Kim, S. Cho, H. Lee, C. Hwang, E.-R. Hwang, J. Song, S. Chae, Y. Chun, J.-K. Kim, High-performance, cost-effective 2z nm two-deck cross-point memory integrated by self-align scheme for 128 Gb SCM, in *Proceedings of the 2018 IEEE International Electron Devices Meeting (IEDM)* (IEEE, 2018), pp. 37.1.1–37.1.4.
15. K. Fulcher, H. Gibb, Setting the research agenda on the health effects of chemicals. *Int. J. Environ. Res. Public Health* **11**, 1049–1057 (2014).
16. A. Verdy, G. Navarro, V. Sousa, P. Noe, M. Bernard, F. Fillot, G. Bourgeois, J. Garrione, L. Perniola, Improved electrical performance thanks to Sb and N doping in SeRich GeSe-based OTS selector devices, in *Proceedings of the 2017 IEEE International Memory Workshop (IMW)* (IEEE, 2017), pp. 1–4.
17. A. Verdy, G. Navarro, M. Bernard, S. Chevalliez, N. Castellani, E. Nolot, J. Garrione, P. Noe, G. Bourgeois, V. Sousa, M.-C. Cyrille, E. Nowak, Carbon electrode for Ge-Se-Sb based OTS selector for ultra low leakage current and outstanding endurance, in *Proceedings of the 2018 IEEE International Reliability Physics Symposium (IRPS)* (IEEE, 2018), vol. 2018, pp. 6D.4-1–6D.4-6.
18. A. Verdy, G. Navarro, M. Bernard, P. Noe, G. Bourgeois, J. Garrione, M.-C. Cyrille, V. Sousa, E. Nowak, High temperature stability and performance analysis of N-doped Ge-Se-Sb based OTS selector devices, in *Proceedings of the 2018 IEEE International Memory Workshop (IMW)* (IEEE, 2018), pp. 1–4.
19. S.-D. Kim, H.-W. Ahn, S. y. Shin, D. S. Jeong, S. H. Son, H. Lee, B.-k. Cheong, D. W. Shin, S. Lee, Effect of Ge concentration in Ge_{1-x}S_x chalcogenide glass on the electronic structures and the characteristics of ovonic threshold switching (OTS) devices. *ECS Solid State Lett.* **2**, Q75–Q77 (2013).
20. S.-Y. Shin, J. M. Choi, J. Seo, H.-W. Ahn, Y. G. Choi, B. Cheong, S. Lee, The effect of doping Sb on the electronic structure and the device characteristics of Ovonic Threshold Switches based on Ge-Se. *Sci. Rep.* **4**, 7099 (2015).
21. J.-Y. Raty, M. Schumacher, P. Golub, V. L. Deringer, C. Gatti, M. Wuttig, A quantum-mechanical map for bonding and properties in solids. *Adv. Mater.* **31**, 1806280 (2019).
22. M. Wuttig, V. L. Deringer, X. Gonze, C. Bichara, J.-Y. Raty, Incipient metals: Functional materials with a unique bonding mechanism. *Adv. Mater.* **30**, e1803777 (2018).
23. H. Y. Cheng, W. C. Chien, I. T. Kuo, E. K. Lai, Y. Zhu, J. L. Jordan-Sweet, A. Ray, F. Carta, F. M. Lee, P. H. Tseng, M. H. Lee, Y. Y. Lin, W. Kim, R. Bruce, C. W. Yeh, C. H. Yang, M. Brightsky, H. L. Lung, An ultra high endurance and thermally stable selector based on TeAsGeSiSe chalcogenides with BEOL IC integration for cross-point PCM, in *Proceedings of the 2017 IEEE International Electron Devices Meeting (IEDM)* (IEEE, 2017), vol. 1, p. 2.2.1–2.2.4.
24. A. Verdy, M. Bernard, J. Garrione, G. Bourgeois, M. C. Cyrille, E. Nolot, N. Castellani, P. Noe, C. Socquet-Clerc, T. Magis, G. Sassine, G. Molas, G. Navarro, E. Nowak, Optimized reading window for crossbar arrays thanks to Ge-Se-Sb-N-based OTS selectors, in *Proceedings of the 2018 IEEE International Electron Devices Meeting (IEDM)* (IEEE, 2018), pp. 37.4.1–37.4.4.

25. R. K. Pan, H. Z. Tao, J. Z. Wang, J. Y. Wang, H. F. Chu, T. J. Zhang, D. F. Wang, X. J. Zhao, Structure and optical properties of amorphous Ge–Se films prepared by pulsed laser deposition. *Optik* **124**, 4943–4946 (2013).
26. W. Zhou, M. Paesler, D. E. Sayers, Structure of germanium-selenium glasses: An x-ray-absorption fine-structure study. *Phys. Rev. B* **43**, 2315–2321 (1991).
27. P. S. Salmon, Structure of liquids and glasses in the Ge–Se binary system. *J. Non Cryst. Solids* **353**, 2959–2974 (2007).
28. C. Yildirim, M. Micoulaut, P. Boolchand, I. Kantor, O. Mathon, J.-P. Gaspard, T. Irifune, J.-Y. Raty, Universal amorphous-amorphous transition in $\text{Ge}_x\text{Se}_{100-x}$ glasses under pressure. *Sci. Rep.* **6**, 27317 (2016).
29. M. Micoulaut, A. Kachmar, M. Bauchy, S. Le Roux, C. Massobrio, M. Boero, Structure, topology, rings, and vibrational and electronic properties of $\text{Ge}_x\text{Se}_{1-x}$ glasses across the rigidity transition: A numerical study. *Phys. Rev. B* **88**, 054203 (2013).
30. C. Massobrio, A. Pasquarello, Structural properties of amorphous GeSe_2 . *J. Phys. Condens. Matter* **19**, 415111 (2007).
31. M. Kibalchenko, J. R. Yates, C. Massobrio, A. Pasquarello, Structural composition of first-neighbor shells in GeSe_2 and GeSe_4 glasses from a first-principles analysis of NMR chemical shifts. *J. Phys. Chem. C* **115**, 7755–7759 (2011).
32. I. Chambouleyron, A. R. Zanatta, Nitrogen in germanium. *J. Appl. Phys.* **84**, 1–30 (1998).
33. F. Boscherini, A. Filippini, S. Pascarelli, F. Evangelisti, S. Mobilio, F. C. Marques, I. Chambouleyron, Short-range order in amorphous germanium-nitrogen alloys studied by extended x-ray-absorption fine-structure spectroscopy. *Phys. Rev. B* **39**, 8364–8370 (1989).
34. I. Pethes, R. Chahal, V. Nazabal, C. Prestipino, A. Trapananti, S. Michalik, P. Jónvári, Chemical short-range order in selenide and telluride glasses. *J. Phys. Chem. B* **120**, 9204–9214 (2016).
35. R. Kaur, P. Singh, K. Singh, A. Kumar, A. Thakur, Optical band gap tuning of Sb-Se thin films for xerographic based applications. *Superlattices Microstruct.* **98**, 187–193 (2016).
36. J. Y. Raty, W. Zhang, J. Luckas, C. Chen, R. Mazzarello, C. Bichara, M. Wuttig, Aging mechanisms in amorphous phase-change materials. *Nat. Commun.* **6**, 7467 (2015).
37. S. Gabardi, S. Caravati, G. C. Sosso, J. Behler, M. Bernasconi, Microscopic origin of resistance drift in the amorphous state of the phase-change compound GeTe. *Phys. Rev. B* **92**, 054201 (2015).
38. P. Noé, C. Sabbione, N. Castellani, G. Veux, G. Navarro, V. Sousa, F. Hippert, F. D'Acapito, Structural change with the resistance drift phenomenon in amorphous GeTe phase change materials' thin films. *J. Phys. D Appl. Phys.* **49**, 035305 (2016).
39. F. Zipoli, D. Krebs, A. Curioni, Structural origin of resistance drift in amorphous GeTe. *Phys. Rev. B* **93**, 115201 (2016).
40. P. Noé, F. Hippert, *Phase Change Memory: Device Physics, Reliability and Applications* (Springer, 2018), pp. 125–179.
41. J.-Y. Raty, P. Noé, G. Ghezzi, S. Maitrejean, C. Bichara, F. Hippert, Vibrational properties and stabilization mechanism of the amorphous phase of doped GeTe. *Phys. Rev. B* **88**, 014203 (2013).
42. M. Micoulaut, J.-Y. Raty, C. Otjacques, C. Bichara, Understanding amorphous phase-change materials from the viewpoint of Maxwell rigidity. *Phys. Rev. B* **81**, 174206 (2010).
43. J. Yoo, Y. Koo, S. A. Chekol, J. Park, J. Song, H. Hwang, Te-based binary OTS selectors with excellent selectivity ($>10^5$), endurance ($>10^8$) and thermal stability ($>450^\circ\text{C}$), in *Proceedings of the 2018 IEEE Symposium on VLSI Technology* (IEEE, 2018), vol. 20, pp. 207–208.
44. T. H. Lee, D. Loke, S. R. Elliott, Microscopic mechanism of doping-induced kinetically constrained crystallization in phase-change materials. *Adv. Mater.* **27**, 5477–5483 (2015).
45. H. Li, J. Robertson, Materials selection and mechanism of non-linear conduction in chalcogenide selector devices. *Sci. Rep.* **9**, 1867 (2019).
46. K. Shportko, S. Kremers, M. Woda, D. Lencer, J. Robertson, M. Wuttig, Resonant bonding in crystalline phase-change materials. *Nat. Mater.* **7**, 653–658 (2008).
47. B. Huang, J. Robertson, Bonding origin of optical contrast in phase-change memory materials. *Phys. Rev. B* **81**, 081204 (2010).
48. P. Zalden, F. Quirin, M. Schumacher, J. Siegel, S. Wei, A. Koc, M. Nicoul, M. Trigo, P. Andreasson, H. Enquist, M. J. Shu, T. Pardini, M. Chollet, D. Zhu, H. Lemke, I. Ronneberger, J. Larsson, A. M. Lindenberg, H. E. Fischer, S. Hau-Riege, D. A. Reis, R. Mazzarello, M. Wuttig, K. Sokolowski-Tinten, Femtosecond x-ray diffraction reveals a liquid–liquid phase transition in phase-change materials. *Science* **364**, 1062–1067 (2019).
49. Q. Xia, J. J. Yang, Memristive crossbar arrays for brain-inspired computing. *Nat. Mater.* **18**, 309–323 (2019).
50. M. Suri, O. Bichler, D. Querlioz, B. Traoré, O. Cuetto, L. Perniola, V. Sousa, D. Vuillaume, C. Gamrat, B. DeSalvo, Physical aspects of low power synapses based on phase change memory devices. *J. Appl. Phys.* **112**, 054904 (2012).
51. P. Němec, A. Moreac, V. Nazabal, M. Pavlišta, J. Příkryl, M. Frumar, Ge–Sb–Te thin films deposited by pulsed laser: An ellipsometry and Raman scattering spectroscopy study. *J. Appl. Phys.* **106**, 103509 (2009).
52. F. Abdel-Wahab, A. Badawi, M. S. Alatibi, S. E. Alomairy, N. N. Ali karar, I. M. Ashraf, E. M. Ahmed, Spectroscopic ellipsometry characterization of $\text{Ge}_{30-x}\text{Sb}_x\text{Se}_{70}$ films using combinations of multiple dispersion functions. *Optik* **147**, 59–71 (2017).
53. J. Orava, T. Wágner, J. Šik, J. Příkryl, M. Frumar, L. Beneš, Optical properties and phase change transition in $\text{Ge}_2\text{Sb}_2\text{Te}_5$ flash evaporated thin films studied by temperature dependent spectroscopic ellipsometry. *J. Appl. Phys.* **104**, 043523 (2008).
54. T. Halenkovič, J. Gutwirth, P. Němec, E. Baudet, M. Specht, Y. Gueguen, J.-C. Sangleboeuf, V. Nazabal, Amorphous Ge-Sb-Se thin films fabricated by co-sputtering: Properties and photosensitivity. *J. Am. Ceram. Soc.* **101**, 2877–2887 (2018).
55. Z. Černošek, E. Černošková, M. Hejdrová, J. Holubová, R. Todorov, The properties and structure of GeSeTe glasses and thin films. *J. Non Cryst. Solids* **460**, 169–177 (2017).
56. F. d'Acapito, G. O. Lepore, A. Puri, A. Laloni, F. La Manna, E. Dettona, A. De Luisa, A. Martin, The LISA beamline at ESRF. *J. Synchrotron Radiat.* **26**, 551–558 (2019).
57. B. Ravel, M. Newville, ATHENA, ARTEMIS, HEPHAESTUS: Data analysis for x-ray absorption spectroscopy using IFEFFIT. *J. Synchrotron Radiat.* **12**, 537–541 (2005).
58. G. Kresse, J. Hafner, Ab initio molecular-dynamics simulation of the liquid-metal–amorphous-semiconductor transition in germanium. *Phys. Rev. B* **49**, 14251–14269 (1994).
59. J. P. Perdew, K. Burke, M. Ernzerhof, Generalized gradient approximation made simple. *Phys. Rev. Lett.* **77**, 3865–3868 (1996).
60. G. Kresse, D. Joubert, From ultrasoft pseudopotentials to the projector augmented-wave method. *Phys. Rev. B* **59**, 1758–1775 (1999).
61. P. E. Blöchl, Projector augmented-wave method. *Phys. Rev. B* **50**, 17953–17979 (1994).
62. J. Heyd, G. E. Scuseria, M. Ernzerhof, Hybrid functionals based on a screened Coulomb potential. *J. Chem. Phys.* **118**, 8207–8215 (2003).
63. X. Gonze, C. Lee, Dynamical matrices, Born effective charges, dielectric permittivity tensors, and interatomic force constants from density-functional perturbation theory. *Phys. Rev. B* **55**, 10355 (1997).

Acknowledgments: XAS measurements with synchrotron radiation were performed at the BM08/LISA beamline of the European synchrotron (ESRF) thanks to beamtimes under experience numbers 08-01-1037/MA-3993/MA-3995. We also sincerely acknowledge G. Bourgeois for invaluable help in the technological lots in LETI clean rooms. **Funding:** This work has been partially supported by the European 621217 PANACHE Project and ANR under contract SESAME ANR-15-CE24-0021. J.-Y.R. acknowledges computational resources provided by CEA-LETI, the CÉCI funded by the F.R.S.-FNRS under grant number 2.5020.11, and the Tier-1 CWB supercomputer infrastructure (Walloon Region under grant agreement number 1117545). J.-Y.R. acknowledges support from the Communauté Française de Belgique through an ARC grant (AIMED 15/19-09). **Author contributions:** P.N. conceptualized the project and experiments with the help of A.V. M.B. prepared the thin-film samples in LETI clean rooms. G.N. supervised the OTS device fabrication in LETI 200-mm technological platform with the help of M.B. A.V. performed and analyzed all electrical measurements in OTS devices with support of G.N. J.-B.D. performed all spectroscopic ellipsometry measurements and data modeling under the supervision of P.N. XAS measurements were performed by A.V., J.-B.J., J.-B.D., P.N., and F.d'A. The XAS and EXAFS data were analyzed by F.d'A. with support from A.V., P.N., and J.-Y.R. The paper was written by P.N. and J.-Y.R. with the help of A.V., F.d'A., and J.-B.D. All AIMD/DFT calculations were performed by J.-Y.R. with the help of P.N. J.G. contributed valuably to the OTS switching model. All authors gave their approval to the final version of the manuscript. **Competing interests:** The authors declare that they have no competing interests. **Data and materials availability:** All data needed to evaluate the conclusions in the paper are present in the paper and/or the Supplementary Materials. Additional data related to this paper may be requested from the authors.

Submitted 5 June 2019
Accepted 21 November 2019
Published 28 February 2020
10.1126/sciadv.aay2830

Citation: P. Noé, A. Verdy, F. d'Acapito, J.-B. Dory, M. Bernard, G. Navarro, J.-B. Jager, J. Gaudin, J.-Y. Raty, Toward ultimate nonvolatile resistive memories: The mechanism behind ovonic threshold switching revealed. *Sci. Adv.* **6**, eaay2830 (2020).

Toward ultimate nonvolatile resistive memories: The mechanism behind ovonic threshold switching revealed

Pierre Noé, Anthonin Verdy, Francesco d'Acapito, Jean-Baptiste Dory, Mathieu Bernard, Gabriele Navarro, Jean-Baptiste Jager, Jérôme Gaudin and Jean-Yves Raty

Sci Adv **6** (9), eaay2830.
DOI: 10.1126/sciadv.aay2830

ARTICLE TOOLS

<http://advances.sciencemag.org/content/6/9/eaay2830>

SUPPLEMENTARY MATERIALS

<http://advances.sciencemag.org/content/suppl/2020/02/24/6.9.eaay2830.DC1>

REFERENCES

This article cites 54 articles, 2 of which you can access for free
<http://advances.sciencemag.org/content/6/9/eaay2830#BIBL>

PERMISSIONS

<http://www.sciencemag.org/help/reprints-and-permissions>

Use of this article is subject to the [Terms of Service](#)

Science Advances (ISSN 2375-2548) is published by the American Association for the Advancement of Science, 1200 New York Avenue NW, Washington, DC 20005. The title *Science Advances* is a registered trademark of AAAS.

Copyright © 2020 The Authors, some rights reserved; exclusive licensee American Association for the Advancement of Science. No claim to original U.S. Government Works. Distributed under a Creative Commons Attribution NonCommercial License 4.0 (CC BY-NC).